

Scale-resolving simulations and investigations of the flow in a hydraulic retarder considering cavitation*

Xue-song LI¹, Qing-tao WU¹, Li-ying MIAO¹, Yu-ying YAN^{†‡2,3}, Chun-bao LIU^{†‡4}

¹State Key Laboratory of Automotive Simulation and Control, College of Automotive Engineering, Jilin University, Changchun 130022, China

²Fluids and Thermal Engineering Research Group, Faculty of Engineering, University of Nottingham, Nottingham NG7 2RD, UK

³Centre for Fluids & Thermal Engineering Research, University of Nottingham, Ningbo 315100, China

⁴School of Mechanical and Aerospace Engineering, Jilin University, Changchun 130022, China

[†]E-mail: yuying.yan@nottingham.ac.uk; liuchunbao@jlu.edu.cn

Received Sept. 15, 2019; Revision accepted Mar. 16, 2020; Crosschecked Sept. 16, 2020

Abstract: Cavitation has a significant influence on the accurate control of the liquid filling rate and braking performance of a hydraulic retarder; however, previous studies of the flow field in hydraulic retarders have provided insufficient information in terms of considering cavitation. Here, the volume of fluid (VOF) method and a scale-resolving simulation (SRS) were employed to numerically and more comprehensively calculate and analyze the flow field in a retarder considering the cavitation phenomenon. The numerical models included the improved delayed detached eddy simulation (IDDES) model, stress-blended eddy simulation (SBES) model, dynamic large eddy simulation (DLES) model, and shear stress transport (SST) model in the Reynolds-averaged Navier-Stokes (RANS) model. All the calculations were typically validated by the brake torque in the impeller rather than the internal flow. The unsteady flow field indicated that the SBES and DLES models could better capture unsteady flow phenomena, such as the chord vortex. The SBES and DLES models could also better capture bubbles than the SST and IDDES models. Since the braking torque error of the SBES model was the smallest, the transient variation of the bubble volume fraction over time on a typical flow surface was analyzed in detail with the SBES model. It was found that bubbles mainly appeared in the center area of the blade suction surface, which coincided with the experiments. The accumulation of bubbles resulted in a larger bubble volume fraction in the center of the blade over time. In addition, the temperature variations of the pressure blade caused by heat transfer were further analyzed. More bubbles precipitated in the center of the blade, leading to a lower temperature in this area.

Key words: Scale-resolving simulation (SRS); Hydraulic retarder; Cavitation; Unsteady flow
<https://doi.org/10.1631/jzus.A1900466>

CLC number: TH137.331


1 Introduction

The hydraulic retarder is a promising auxiliary brake system in commercial vehicles and its working

principle is shown in Fig. 1. The basic components of a hydraulic retarder include a rotor, stator, transmission shaft, heat exchanger, and charge control mechanism which includes a regulating valve and storage tank. The hydraulic loss of fluid and fluid impact on the stator blades when transmission oil circulates between the rotor and stator are the main causes of braking torque. There exist high pressure and low pressure areas during the high-speed operation of a retarder; the bubbles are present and cavitation erosion is often happening in the retarder. The cavitation mechanism in the retarder is firstly introduced in the following. At a certain temperature of the transmission oil, when the local low pressure of the

* Corresponding author

[†] Project supported by the Key Scientific and Technological Project of Jilin Province (No. 20170204066GX), the Natural Science Foundation of Jilin Province (No. 20200201222JC), the Science and Technology Project of Jilin Provincial Education Department (No. JJKH20170785KJ), the Project of Jilin Provincial Science & Technology Department (No. 20200301011RQ), and the Advanced Manufacturing Projects of Government and University Co-construction Program funded by Jilin Province (No. SXGJSF2017-2), China

 ORCID: Chun-bao LIU, <https://orcid.org/0000-0002-8265-2875>

© Zhejiang University and Springer-Verlag GmbH Germany, part of Springer Nature 2020

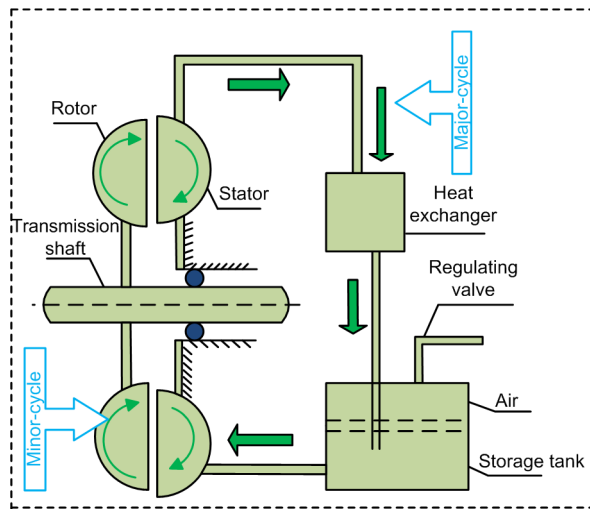


Fig. 1 Working principle of hydraulic retarder

flow field drops to the saturation vapor pressure of this temperature, bubbles will be generated and will collapse as they flow to the high-pressure zone. This results in a fluid impact and noise. Therefore, it is important to study the cavitation flow field of the retarder, and this lays the foundation for the next step, i.e. proposing measures to reduce cavitation erosion. The first step to study cavitation flow field is researching the turbulent flow field of the retarder. Up to now, scholars have been devoted to the simulation of the flow field inside a hydraulic retarder, laying the foundation for our research to investigate the flow field considering cavitation. Zheng et al. (2016, 2017a, 2017b, 2018) simulated the fluid flow and heat transfer inside a retarder using the Reynolds-averaged Navier-Stokes (RANS) and transition shear stress transport (SST) models. The results showed that the simulation ability of the transition SST model was better than that of the RANS model. A two-phase flow of a hydraulic retarder based on the RANS model was simulated in 2018 and the velocity vector distribution of different filling rates and different detection positions was also analyzed (Hur et al., 2018). In comparison with the RANS method, a hybrid RANS/LES (HRL) simulation applies the RANS model in the boundary layer region and the large eddy simulation (LES) model in the turbulent core region and can better capture the turbulent flow characteristics. In the comparative studies carried out by Liu et al. (2017a, 2017b), the improved delayed detached eddy simulation (IDDES), the stress-blended eddy simulation (SBES), and the dynamic large eddy sim-

ulation (DLES) models in an HRL have the ability to capture the vortex characteristics at the interface, while the RANS model failed to capture these characteristics (Liu et al., 2017a).

The above turbulent flow studies lay the foundation for the following cavitation flow studies. From the above studies, it was revealed that the current cavitation phenomenon is often neglected when studying the retarder flow field and it results in a 5%–15% energy and efficiency loss (Mejri et al., 2006). The cavitation phenomenon also affects the precise control of the liquid filling rate and causes vibration and noise throughout the entire transmission system. Therefore, it is necessary to introduce a cavitation model to simulate the cavitation flow field inside a hydraulic retarder. In the literature review, though cavitation studies have rarely been reported in retarders, they have been extensively reported in other fluid machinery, such as pumps, variable cross-section pipes, and torque converters. A new method for the analysis of cavitation behaviour was presented and applied to study the cavitation behaviour of a large storage pump (Stuparu et al., 2010). The cavitation flow field of a torque converter with different pump speeds was theoretically simulated in 2002. All of the results demonstrated that when the transmission ratio reached 0, large volumes of bubbles obstructed the flow passage causing the torque ratio and torque capacity to decrease drastically (Dong et al., 2002a, 2002b). Watanabe et al. (2012) experimentally studied the flow field in a torque converter with cavitation and vibration phenomena. A recording from a high-speed camera showed that bubbles appeared at the edge of the converter blade when the cavitation number reached 1.65, and when the cavitation number decreased to 1.25, the number of bubbles in the flow field increased and the value of the torque obtained by the torque sensor was also low. A study of the vibration frequency of the entire system also found that cavitation was also the main cause of the high-frequency vibration in the system. In our area of interest, a mathematical model to predict cavitation based on the plane fitting method was proposed in 2008, which can be used for a torque converter with a similar design (Robinette et al., 2008a, 2008b). Long et al. (2017) used the modified renormalization group turbulence model with a local density correction to study unsteady cavitating turbulent flow in liquid hydrogen and found that the motion of bubbles was

related to the vortex in the flow field. Snigerev et al. (2017) set monitoring points in flow fields of different cross-sections and revealed the law of cavitation motion by studying the pressure and the bubble volume distribution. The study revealed that the initiation of the cavity was caused by a local low pressure. Tsutsumi et al. (2017) found that the cavitation of a torque converter was most severe when the speed ratio reached 0 and the cavitation number was less than 1. The bubbles generated by the cavitation caused the torque transmitted by the torque converter to drop dramatically.

In this study, we adopt a scale-resolving simulation (SRS) to investigate the flow field in a hydraulic retarder considering cavitation by means of ANSYS FLUENT software. The volume of fluid (VOF) two-phase flow model and the Schnerr and Sauer cavitation model are employed, while the representative IDDES, SBES, and DLES models are selected for the turbulence model in the SRS, and the SST $k-\omega$ model in the RANS model is used for a comparison with the same grid. In this way, the abilities of different turbulence models to calculate the flow field are analyzed and compared. We aim to research the flow field inside the hydraulic retarder considering cavitation, and provide some insight for subsequent structural optimization of retarders.

2 Computational model

2.1 VOF model

The VOF can model two or more immiscible fluids by solving a single set of momentum equations and tracking well the volume fraction of each phase; hence, the VOF is employed to simulate the two-phase flow of the hydraulic retarder. The tracking of the interface between the oil-vapor phase is accomplished by a solution of the continuity equation for the volume fraction of each phase. The control continuity equation for the q th fluid is as follows:

$$\frac{1}{\rho_q} \left[\frac{\partial}{\partial t} (\alpha_q \rho_q) + \frac{\partial}{\partial x_j} (\alpha_q \rho_q u_j) \right] = S_{\alpha_q} + \sum_{p=1}^{n_{\text{phase}}} (\dot{m}_{pq} - \dot{m}_{qp}), \quad (1)$$

where t is the time, α_q and ρ_q are the volume fraction and density for the q th fluid, and \dot{m}_{pq} and \dot{m}_{qp} are the mass transfer rates for the p th fluid to the q th fluid and

the q th fluid to the p th fluid, respectively. x_j and u_j represent a coordinate axis and the corresponding speed, respectively. n_{phase} is the number of phases except vapor phase. The mass transfer rate between the oil and vapor is derived by the cavitation model in Section 2.2. S_{α_q} is a user-defined mass source term.

Eq. (1) is the continuity equation for the q th fluid and it is derived from the mass conservation equation for a fluid. It says that for every phase fluid, the increase in the mass of the fluid of micro-element per unit time is equal to the sum of the net mass flowing into the micro-element.

2.2 Cavitation model

There are many nuclei for the inception of cavitation in most situations, so the primary focus is on properly accounting for the bubble growth and collapse (Huang and Wang, 2011; Luo et al., 2016). The bubble dynamics equation can be derived from the Rayleigh-Plesset equation (Brennen, 1995):

$$R_b \frac{d^2 R_b}{dt^2} + \frac{3}{2} \left(\frac{dR_b}{dt} \right)^2 = \frac{p_b - p}{\rho_l} - \frac{4\nu_l}{R_b} \frac{dR_b}{dt} - \frac{2\sigma}{\rho_l R_b}, \quad (2)$$

where p_b and p are the internal and external pressures of the bubble, respectively. R_b is the radius of the bubble, ν_l is the kinematic viscosity of the oil phase, ρ_l is the density of the oil phase, and σ is the tension coefficient of the oil-air surface. Eq. (2) is simplified to Eq. (3) when the 2nd-order term and the surface force are ignored:

$$\frac{dR_b}{dt} = \sqrt{\frac{2}{3} \frac{p_b - p}{\rho_l}}. \quad (3)$$

Eq. (3) provides a physical approach to visualize the dynamics of bubbles in a cavitation model. The software ANSYS FLUENT provides three cavitation models: the Singhal model (Singhal et al., 2002), Zwart-Gerber-Belamri model (Zwart et al., 2004), and the Schnerr and Sauer model (Schnerr and Sauer, 2001). The last model considers the phase transition, the dynamic motion of the bubbles, and the pressure fluctuation of the turbulent flow field. As a result, this model has good ability to simulate the oil-to-air phase transportation problem. Therefore, we adopt this model, and the typical form of the vapor phase of the oil control equation is shown as

$$\frac{\partial}{\partial t}(\alpha_v \rho_v) + \frac{\partial}{\partial x_j}(\alpha_v \rho_v u_j) = \frac{\rho_v \rho_l}{\rho_m} \frac{d\alpha_v}{dt}, \quad (4)$$

where the subscripts v, l, and m in the equation represent the vapor phase, liquid phase, and mixing phase for oil, respectively, and the right term of the equation is the mass transfer term, which is equal to the right term of Eq. (1):

$$\sum_{p=1}^{n_{\text{phase}}} (\dot{m}_{pq} - \dot{m}_{qp}) = \frac{\rho_v \rho_l}{\rho_m} \frac{d\alpha_v}{dt}. \quad (5)$$

To solve the above equation, we adopt Eq. (6) to relate the bubble volume fraction α_v in Eq. (5) and the number of bubbles n_b :

$$\alpha_v = \frac{n_b \frac{4}{3} \pi R_b^3}{1 + n_b \frac{4}{3} \pi R_b^3}. \quad (6)$$

From the above discussion, the mass transfer term is derived by Eqs. (1), (5), and (6):

$$\sum_{p=1}^{n_{\text{phase}}} (\dot{m}_{pq} - \dot{m}_{qp}) = \frac{\rho_v \rho_l}{\rho_m} \alpha_v (1 - \alpha_v) \frac{3}{R_b} \sqrt{\frac{2}{3} \frac{p_b - p}{\rho_l}}. \quad (7)$$

2.3 Turbulence model

2.3.1 SST k - ω model

The turbulent kinetic energy (k) equation and specific dissipation rate (ω) equation are expressed as follows (Orszag et al., 1993; Menter, 1994):

$$\begin{aligned} \frac{\partial}{\partial t}(\rho k) + \frac{\partial}{\partial x_j}(\rho k u_j) &= \frac{\partial}{\partial x_j} \left[(\mu + \sigma_k \mu_t) \frac{\partial k}{\partial x_j} \right] \\ &+ \mu_t \frac{\partial u_i}{\partial x_j} \left(\frac{\partial u_i}{\partial x_j} + \frac{\partial u_j}{\partial x_i} \right) - \beta^* \rho k \omega, \end{aligned} \quad (8)$$

$$\begin{aligned} \frac{\partial}{\partial t}(\rho \omega) + \frac{\partial}{\partial x_j}(\rho \omega u_j) &= \frac{\partial}{\partial x_j} \left[(\mu + \sigma_\omega \mu_t) \frac{\partial \omega}{\partial x_j} \right] \\ &+ \alpha \rho S^2 - \beta \rho \omega^2 + 2(1 - F_1) \frac{\rho \sigma_{\omega 2}}{\omega} \frac{\partial k}{\partial x_j} \frac{\partial \omega}{\partial x_j}, \end{aligned} \quad (9)$$

where μ is the dynamic viscosity, x_i and u_i represent a coordinate axis and the corresponding speed, respec-

tively, S is the strain rate, and σ_k , σ_ω , $\sigma_{\omega 2}$, and β^* are model parameters. The mixing function F_1 is define by

$$F_1 = \tanh \left\{ \min \left[\max \left(\frac{\sqrt{k}}{\beta^* \omega y}, \frac{500 \mu}{\rho y^2 \omega} \right), \frac{4 \rho \sigma_{\omega 2} k}{\text{CD}_{k\omega} y^2} \right] \right\}^4, \quad (10)$$

$$\text{CD}_{k\omega} = \max \left(2 \rho \sigma_{\omega 2} \frac{1}{\omega} \frac{\partial k}{\partial x_j} \frac{\partial \omega}{\partial x_j}, 10^{-10} \right). \quad (11)$$

In the SST k - ω model, the turbulent viscosity μ_t is defined as

$$\mu_t = \frac{\alpha_1 k}{\max(\alpha_1 \omega, SF_2)}, \quad (12)$$

where F_2 is also the mixing function, which is

$$F_2 = \tanh \left[\max \left(\frac{2\sqrt{k}}{\beta^* \omega y}, \frac{500 \mu}{\rho y^2 \omega} \right) \right]^2, \quad (13)$$

where y is the distance from the wall, and the parameters used in the model are as follows:

$$\sigma_k = \sigma_\omega = 0.5, \quad \sigma_{\omega 2} = 1.168, \quad \beta^* = 0.09, \quad \alpha_1 = 0.31. \quad (14)$$

2.3.2 IDDES model

The IDDES model is an extension of the DDES model and proposes a hybrid formulation that switches between the RANS and LES models based on the grid resolution. The switch is based on the following notion:

$$C_{\text{des}} \Delta_{\text{max}} > l_t \rightarrow \text{RANS}, \quad C_{\text{des}} \Delta_{\text{max}} \leq l_t \rightarrow \text{LES}, \quad (15)$$

where C_{des} is a calibration constant of 0.61 that is used in the IDDES model. Δ_{max} is the maximum grid spacing and l_t is the limiter, which are defined by

$$\Delta_{\text{max}} = \max(\Delta_x, \Delta_y, \Delta_z), \quad l_t = \frac{k^{\frac{3}{2}}}{\varepsilon} = \frac{\sqrt{k}}{\beta^* \omega}, \quad (16)$$

where ε is the energy dissipation rate.

2.3.3 SBES model

The SBES model can transform between the RANS and LES models. The SBES model reconstructs the blending function to provide a more reasonable boundary layer protection mechanism to limit premature switching to the LES model. Premature switching can degrade the ability of the RANS model to model the underlying boundary. The SBES model adds a sink term $\varepsilon_{\text{SBES}}$ to the equation, as shown in the following (Menter, 1994):

$$\begin{aligned} \varepsilon_{\text{SBES}} &= -\beta^* \rho k \omega F_{\text{SBES}}, \\ F_{\text{SBES}} &= \max \left(\frac{l_t}{C_{\text{SBES}} \Delta_{\text{SBES}}} (1 - f_s), 1 \right) - 1, \end{aligned} \quad (17)$$

where C_{SBES} is the model parameter, and Δ_{SBES} is the grid size. f_s is used in the blending function to combine the stress term in the SST model and the LES model as follows:

$$\tau_{ij}^{\text{SBES}} = f_s \tau_{ij}^{\text{SST}} + (1 - f_s) \tau_{ij}^{\text{LES}}, \quad (18)$$

where τ_{ij}^{SST} and τ_{ij}^{LES} are the modeling stress tensors for the SST and the LES models, respectively, and τ_{ij}^{SBES} is the stress tensor for the SBES model.

2.3.4 DLES model

The DLES model is an extension of the LES model and can directly calculate the large-scale vortex, while a small-scale vortex can be simulated by

the sub-grid-stress (SGS) models. In this study, the SGS model adopts the Smagorinsky-Lilly model (Smagorinsky, 1963), and the turbulent viscosity in this model is defined by

$$\mu_t = C_s^2 \Delta^2 \sqrt{2 \bar{S}_{ij} \bar{S}_{ij}}, \quad (19)$$

where C_s is a constant with a value of 0.1, and Δ is the subgrid resolution. The SGS stress tensor is given as

$$\mathbf{T}_{ij} = -2\mu_t \bar{S}_{ij} + \frac{1}{3} \mathbf{T}_{kk} \delta_{ij}, \quad (20)$$

where \mathbf{T}_{kk} is the secondary stress tensor. δ_{ij} is a math function: while $i=j$, $\delta_{ij}=1$, else $\delta_{ij}=0$. \bar{S}_{ij} is defined as

$$\bar{S}_{ij} = \frac{1}{2} \left(\frac{\partial \bar{u}_i}{\partial \bar{x}_j} + \frac{\partial \bar{u}_j}{\partial \bar{x}_i} \right). \quad (21)$$

The above has introduced different turbulence models adopted in this study. The advantages and disadvantages of above turbulent models are shown in Table 1.

3 Computational settings and verification

3.1 Mesh layout and simulation settings

Fig. 2 shows the computational domain and grid model of the hydraulic retarder. It is clearly seen that the straight blades are evenly distributed in the rotor

Table 1 Advantages and disadvantages of different turbulence models

Model	Advantage	Disadvantage
SST $k-\omega$	Based on the RANS ideology, the amount of calculation is small, the grid size and accuracy are generally required, and the time-averaging process can effectively calculate the average flow	The calculation error is large, and the ability to capture the vortex is poor
IDDES	It belongs to the HRL algorithm, which comprehensively utilizes the advantages of the RANS and LES methods. It has a strong ability to capture the vortex of the flow field, and the flow field analysis result is accurate	There are large amount of calculations and high requirements for grid accuracy
SBES	It belongs to the HRL algorithm. Compared with IDDES, SBES introduces a hybrid function, the conversion between RANS and LES is more reasonable, and the accuracy of the calculation result is very high	The required mesh size is small, and the requirements for the boundary layer mesh are high
DLES	It belongs to the HRL algorithm, provides numerous SGS models to simulate small-scale vortices, and has a strong ability to capture vortices	The amount of calculation is too large, and the capture of small eddies depends too much on grid accuracy and grid size

and stator, the oil inlet of the retarder is distributed in the center of the stator blades, and the thickness of the blade with the oil inlet is larger than that of the remaining blades to ensure the strength of the material. The outer ring of the stator wall is distributed with the oil outlet. The interface is the intersection area for the rotor and the stator. Table 2 presents the structural parameters of the hydraulic retarder. Considering the differences in the subflow passages of a hydraulic retarder, all domains are meshed with a hexahedron structural grid. The center in Fig. 2 is the full-passage grid of the retarder, with local grid details shown on the left and right. The global maximum size for our grid is 0.05 mm and the expansion ratio is no more than 3. To better capture the flow information, especially the viscous sub-layer, a local-grid refinement is applied to obtain a sufficient resolution. We calculate the boundary layer information for rotor and stator blades. The initial grid spacing can be calculated by (Moshfeghi and Hur, 2015)

$$\Delta y = Ly^+ \sqrt{80} Re_L^{-\frac{13}{14}} = 30 \times 1 \times \sqrt{80} \times 50000^{-\frac{13}{14}} = 0.0116 \text{ mm}, \quad (22)$$

where L is the characteristic length ($L=30$ mm), y^+ is the target value for y plus ($y^+=1$), Re_L is the Reynolds number based on chord length ($Re_L=50000$), and Δy represents the initial grid spacing and the value is 0.0116 mm after calculation. The boundary layer thickness can be calculated by (Moshfeghi and Hur, 2015)

$$\delta_{BL} = 0.035 L Re_L^{-\frac{1}{7}} = 0.035 \times 30 \times 50000^{-\frac{1}{7}} = 0.2238 \text{ mm}, \quad (23)$$

where δ_{BL} represents the boundary layer thickness and the value is 0.2238 mm after calculation. Considering the first grid spacing and boundary layer thickness, the number of layers is 20 in the normal-to-surface direction inside the boundary layer and the calculated y^+ is 1 for the first layer. In our earlier study of a hydraulic retarder, our team carried out the verification of grid dependence and the change rate for braking torque with computational consumptive time was adopted to evaluate the grid dependence (Liu et al., 2017b). It was found that with the increase of grid

number, the change rate of braking torque was decreasing and the computational time was increasing. In our study, when the grid number exceeds 4×10^6 , the change rate of braking torque is within 0.2% and the computational time is 30 h. Thus, combining the change rate of braking torque and computational time, the grid number for the full passage is chosen to be 4×10^6 to carry out our following study.

In the VOF calculation process, the rotor domain is the rotating part, and the stator domain is the fixed part. To enable the flow variables to exchange between the rotating and fixed zones, the sliding mesh method is employed to conduct a numerical simulation. The details of the simulation are shown in Table 3. In our simulation the calculation results were considered to be converged when the change rate for braking torque values in two consecutive iterations was less than 10^{-4} . Furthermore, all normalized residual values in Navier-Stokes equations needed to be less than 10^{-6} . Because heat transfer is accompanied by the cavitation process, to investigate the temperature change with the cavitation, the oil parameter as a function of temperature is taken from our previous study (Liu et al., 2017b).

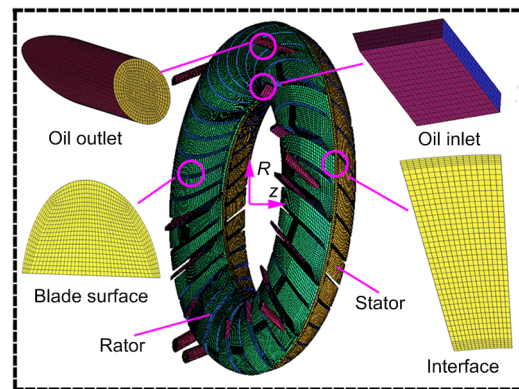


Fig. 2 Structural mesh for hydraulic retarder

Table 2 Structural parameters of retarder

Parameter	Value	
	Rotor	Stator
Effective diameter of circulation circle (mm)	293	296
Number of blades	36	34
Incline angle of the blade (°)	40	40
Wedge angle of the blade (°)	30	30
Number of oil inlets	0	10
Number of oil outlets	0	6

3.2 Comparison between the simulation and experimental data

When a hydraulic retarder operates, the high-speed kinetic energy fluid from the rotor impacts the stationary stator blades to generate a vehicle braking torque. The braking torque can be derived from

$$T_B = \lambda_B \cdot n^2 \cdot D^5, \quad (24)$$

where λ_B is the braking torque coefficient, D is the diameter of circulating circle, n is the rotor speed, and T_B is the braking torque. Eq. (24) shows that the braking torque is proportional to the square of the rotor speed, which can also be concluded from Fig. 3a. Figs. 3b and 3c show the braking torque errors under noncavitation and cavitation conditions,

respectively. The error values of the above models are within 10%, indicating that the four turbulence models have good application prospects in engineering. The

Table 3 Computational fluid dynamics (CFD) model description of retarder

Item	Description
Multiphase model	VOF model
Turbulence model	SST $k-\omega$, IDDES, SBES, and DLES models
Interaction method	Sliding mesh method
Inlet condition	Velocity-inlet with an inlet temperature of 333 K
Outlet condition	Pressure outlet
Pressure-velocity coupling	SIMPLEC
Transient formulation	Bounded 2nd-order implicit
Momentum discretization	2nd-order upwind
Time step size	0.0005 s

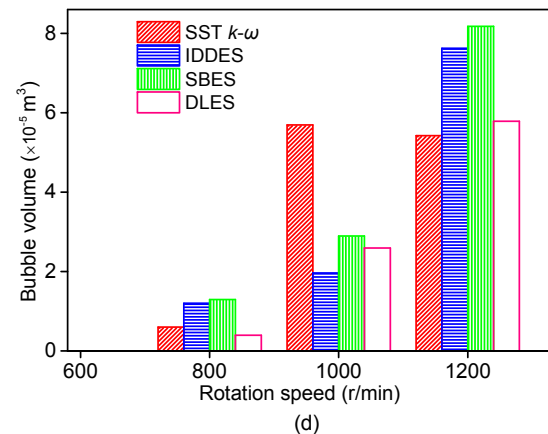
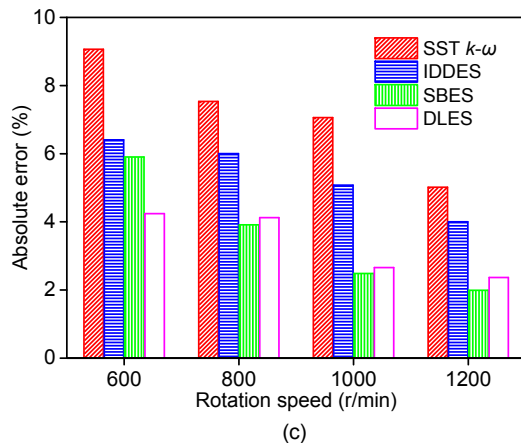
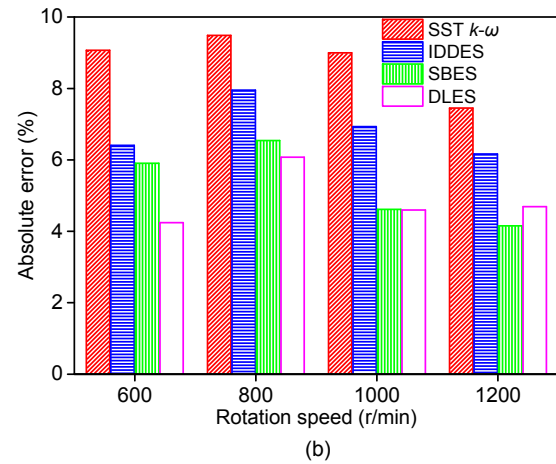
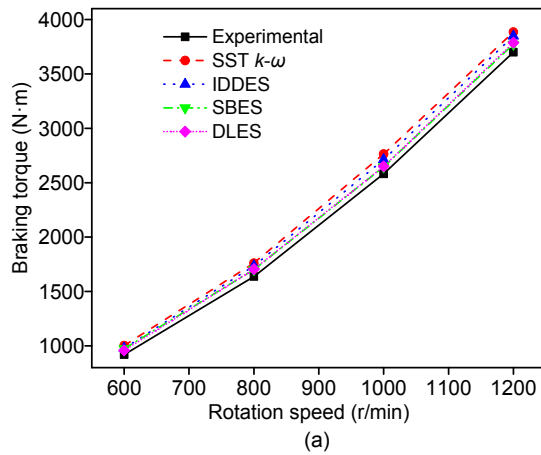


Fig. 3 Comparison studies between the simulation and experimental data for different models

(a) Simulation and experimental braking torques under the cavitation condition; (b) Braking torque errors for different models under the noncavitation condition; (c) Braking torque errors for different models under the cavitation condition; (d) Total bubble volumes of different models under the cavitation condition

error values of the SST $k-\omega$ and IDDES models are larger than those of the SBES and DLES models. It is important that the torque error values considering cavitation are significantly smaller than those without considering cavitation, which indicates that it is better to consider cavitation in a simulation of the unsteady flow field. From the total volume of the bubbles in the flow field at different rotor speeds in Fig. 3d, we see that the bubble precipitation is obvious under the high-speed condition. Since the bubble precipitates the most in the flow field when the rotor speed reaches 1200 r/min, the following sections mainly analyze the flow field under this condition.

4 Simulation results and discussion

4.1 Comparative analysis for velocity components

To compare the differences between the different turbulence models, Figs. 4a–4c extract the velocity components at 25 different points, and the distribution of these 25 points is shown on the left side of Fig. 6. The velocities V_t , V_a , and V_r represent the tangential velocity, axial velocity, and radial velocity, respectively, at the extraction points, and the horizontal axis r/R (R is the effective radius of circulation circle of retarder) is from 0 to 1, representing extraction point 1 to extraction point 25. The four models all show that the velocity direction of the fluid changes between the inner diameter and the outer diameter of the flow field. In addition, a velocity loss is observed in the center part of the flow field. The four turbulence models are consistent in the velocity distribution and velocity values in the simulation of the tangential velocity, and the four turbulence models are also consistent in the axial velocity simulation. However, because the turbulent flow is complex and variable in the radial direction, there are some differences in radial velocities among the four turbulence models. From Fig. 4b, it is shown that the radial velocity of the DLES model in the inner diameter is lower than that of the other three models, and the absolute radial velocity values of the DLES and IDDES models in the outer diameter are lower than those of the SST and SBES models. The reason for this is that the turbulent intensities simulated by DLES and IDDES models are small compared to the other models in the radial flow, as can be seen from Fig. 5c,

where the large viscous force contributes to the low radial velocity. We should be aware that although there are some differences among the simulation results for the different turbulence models, the ability to capture the velocity field is fairly good for them all.

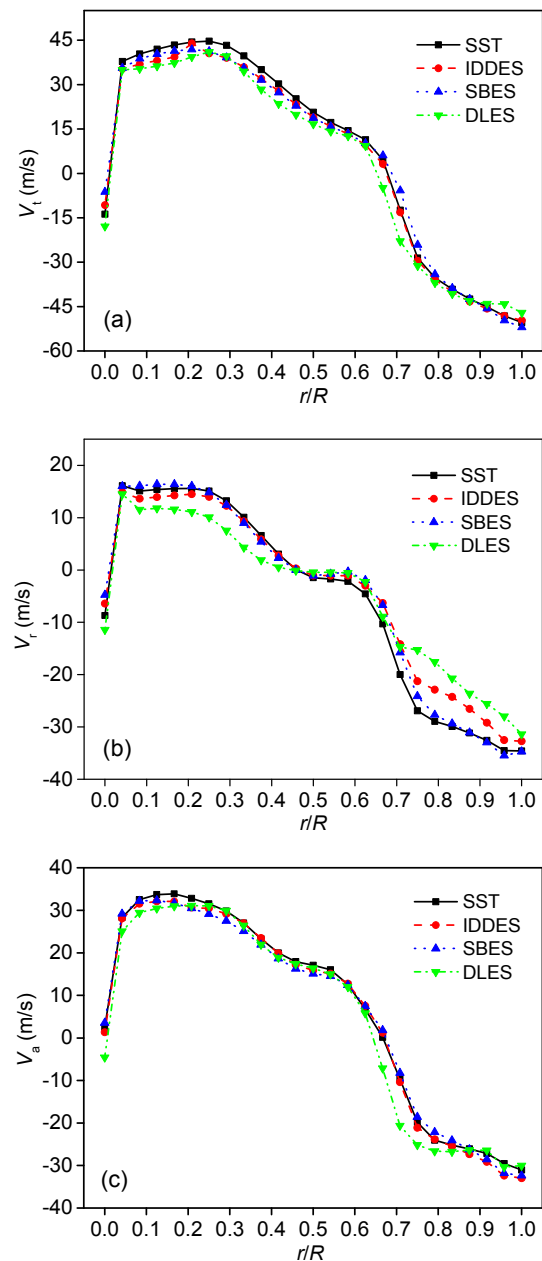


Fig. 4 Comparison of velocity data for different models
(a) Tangential velocity; (b) Radial velocity; (c) Axial velocity

There are some differences in the turbulence simulations for the different models. Figs. 5a–5c analyze the turbulence information of the extracted

points, including turbulent kinetic energy (k), specific dissipation rate (ω), and turbulent viscosity (μ_t). Since the DLES model does not include k and ω , we therefore only compare μ_t . It can be seen from Fig. 5b that the results simulated by the SST, IDDES, and SBES models are roughly the same in terms of the specific dissipation rate, but there is a slight difference: the order of the values is IDDES>SBES>SST as a whole, indicating that there exists a similar order of IDDES>SBES>SST in the energy dissipation. However, there is a noticeable difference in the turbulent kinetic energy: the SST and SBES simulation values are significantly larger than the IDDES simulation values, especially in the wide range of r/R of 0.6–1.0. This is because of the rapid fluid acceleration that occurs by obtaining energy from the rotor. It is known that the turbulent kinetic energy is a measure of the development or decline of turbulence, and the simulation results show that the turbulent flow energy simulated by the SST and SBES models is obviously stronger than that of the IDDES model. In the error maps of Figs. 3b and 3c we find that the SST k - ω model has the maximum errors under both the noncavitation and cavitation conditions when the rotor speed reaches 1200 r/min, so we infer that the SST model overestimates the turbulence intensity. Since the difference between the turbulence models is the calculated value of the turbulent viscosity in the discrete control equations, the turbulent viscosity can be calculated by

$$\mu_t = \frac{\rho k}{\omega}. \quad (25)$$

Therefore, we present the turbulent viscosity of the different models in Fig. 5c. It can be concluded that the SBES- and SST-simulated values are slightly larger than the IDDES-simulated values. These results can be confirmed from the k and ω results in Figs. 5a and 5b and Eq. (25). In addition, the values simulated by the DLES model are the lowest.

4.2 Comparative vortex analysis of the chord surface

In this section, three representative chord surfaces are chosen to analyze the vortex distribution, and the position of the chord surface is shown on the right side of Fig. 6.

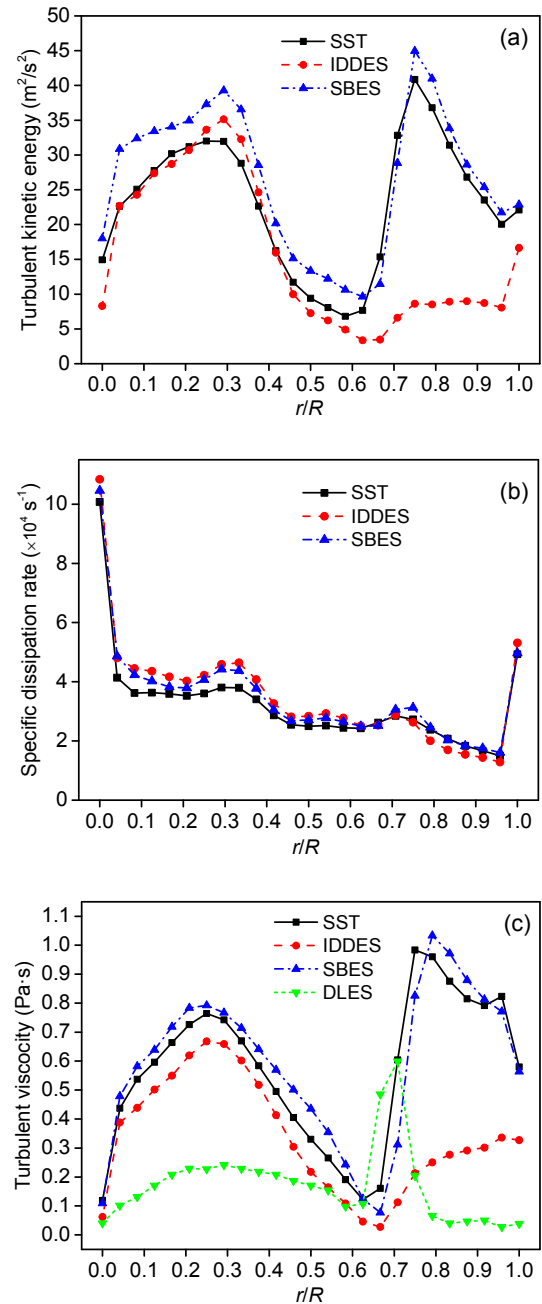


Fig. 5 Comparison of turbulence data for different models

(a) Turbulent kinetic energy; (b) Specific dissipation rate; (c) Turbulent viscosity

It can be seen from the streamline trend in Fig. 7 that the $R=90$ mm chord surface corresponds to the fluid flowing from the stator flow passage to the rotor flow passage. The $R=140$ mm chord surface is exactly the opposite, and the $R=120$ mm chord surface is the interface area. Figs. 7a–7d show a part of the extracted

chord surface flow data. Figs. 7e and 7f are the enlarged views of simulation for the SBES model in the 90-mm and 140-mm chord surfaces, respectively. Through a comparison of the different turbulence models in Figs. 7a–7c, it can be seen that a large vortex exists near the blades, especially at the blade

wedge corners where the fluid viscosity is large, resulting in a large vortex distribution. It is obvious that the simulated vortex values of the SBES and DLES models are larger than those of the SST and IDDES models, indicating that larger vortices are captured in the SBES and DLES simulations; this result indicates that the energy dissipation loss of the SBES and DLES models is larger than those of the SST and IDDES models because of viscous dissipation, so it can be found from the error map in Fig. 3c that the SBES and DLES torque errors are smaller than those of the SST and IDDES models when the rotational speed reaches 1200 r/min. It should be noted that the 120-mm chord surface is the intersection area, and this chord surface is very different from the other two chord surfaces. From the bubble volume fraction of

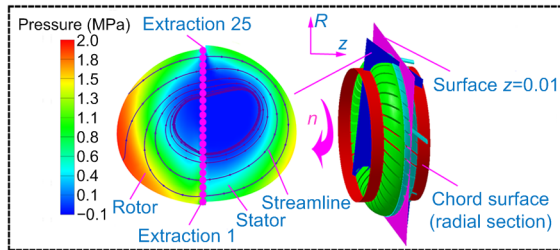


Fig. 6 Extracted surface of the hydraulic retarder

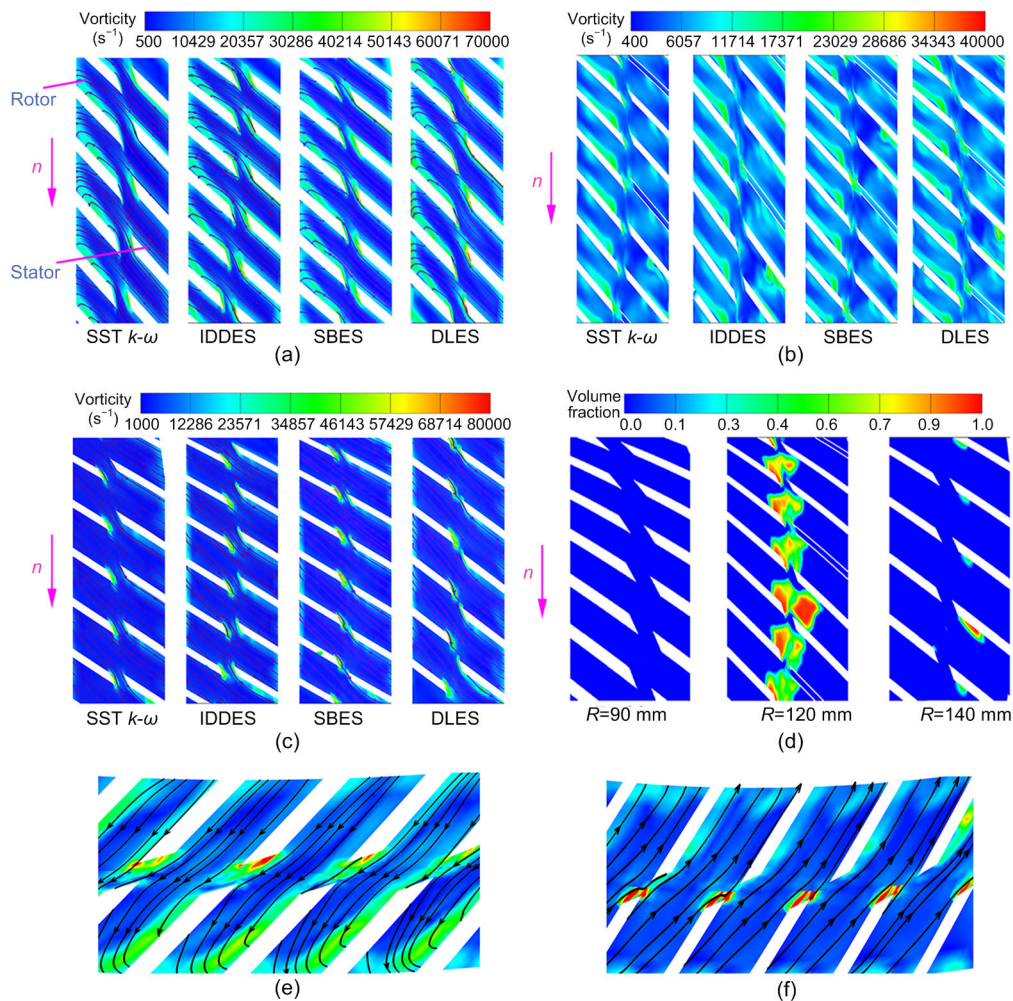


Fig. 7 Vortex and bubble volume fractions of three chord surfaces

(a) $R=90$ mm chord surface; (b) $R=120$ mm chord surface; (c) $R=140$ mm chord surface; (d) Bubble volume fraction of chord surface; (e) Enlarged view of $R=90$ mm SBES model in Fig. 7a; (f) Enlarged view of $R=140$ mm SBES model in Fig. 7c

the three surfaces in Fig. 7d, it can be found that the bubble volume fraction of the 120-mm chord surface is close to 1 in the local region; however, the bubble volume fractions of the other two chord surfaces nearly reach 0, indicating that there exist a large number of bubbles in the 120-mm chord surface. Bubbles can damage the vortex distribution, causing the vortex in Fig. 7b to be significantly smaller than that of the 90-mm and 140-mm chord surfaces in Figs. 7a and 7c, and the high vortex distribution at the blade wedge angle also disappears compared with the other surfaces. The results computed by the different turbulence models are not very different at this chord surface.

5 Analysis of the cavitation flows

From the previous discussion, we conclude that the SBES and DLES models can capture more details of the flow field, and because the SBES model has less torque error than the DLES model when the rotor speed reaches 1200 r/min, this section simulates the transient evolution of the cavitation field over time t based on the SBES model.

5.1 Transient bubble volume fraction evolution analysis on the flow surface

The local low pressure is the direct reason for the existence of bubbles, so there exist some bubbles in the low-pressure region. Fig. 8 shows the variation in the transient bubble volume fraction over time. The bubble volume fraction in the flow field is small at 0.03 s and the bubbles mainly exist in entrance area 1 of the rotor and entrance area 2 of the stator. Since the stator blades are stationary, the flowing fluid has a large pressure loss when the fluid impacts the entrance of the stator blade. The fluid also exhibits a decrease in pressure when flowing out of the stator passage to the rotor passage. From the bubble volume fraction distribution at 0.05 s, it can be found that the volume fraction of the bubbles in the core region is obviously high. It is worth noting that two bubble accumulation areas are formed in the stator flow passage. One area is in entrance area 3 of the stator passage. The bubble volume fraction in the core area is high, approximately 1, in this area. The other area is in area 4, which is below the entrance of the stator flow passage. In this area, the bubble volume fraction

is low, approximately 0.4–0.5. The two aggregating regions gradually expand over time; it is clearly seen that the bubble volume fraction in the core region is close to 1 and that in the peripheral region is relatively low, approximately 0.5, indicating that this region is a region in which the transmission oil and the bubble are uniformly mixed. It is interesting to note that the two bubble accumulation regions appearing in the stator flow passage approach each other and gradually integrate into one area at 0.08 s. However, there are some differences in the rotor bubble accumulation area: there is only one bubble accumulation area and the shape of the area is regular. The accumulation area also gradually expands over time, and the bubble volume fraction of the core area is obviously higher than that of the edge area. As the volume fraction of bubbles is large in the flow passage at 0.05 s, it will have a relatively significant impact on the braking performance and stability of the hydraulic retarder.

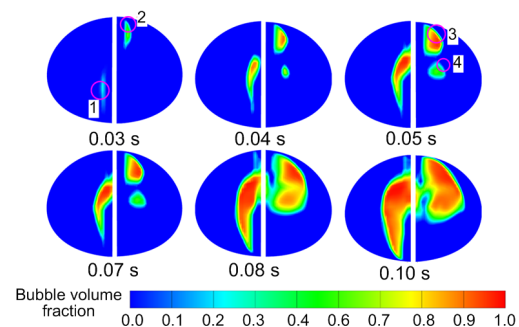


Fig. 8 Bubble volume fraction evolution cloud over time on the flow surface

5.2 Analysis of the cavitation flow data of the axial surface at 0.04 s and 0.10 s

The cavitation flow field changes over time, so this section first analyzes the bubble volume distributions of different axial sections at 0.04 s and 0.10 s. The axial section is shown on the right side of Fig. 6. Fig. 9a shows the bubble distribution on the axial surface at 0.04 s. The cavitation phenomenon is not obvious at 0.04 s and the total number of bubbles in the flow field is small; only the $z=0$ and $z=-0.005$ surfaces have bubbles in the extracted axial section, and the bubble volume fraction is only approximately 0.3. The bubble distribution on the axial surface at 0.10 s in Fig. 9b shows that the bubbles appear on all

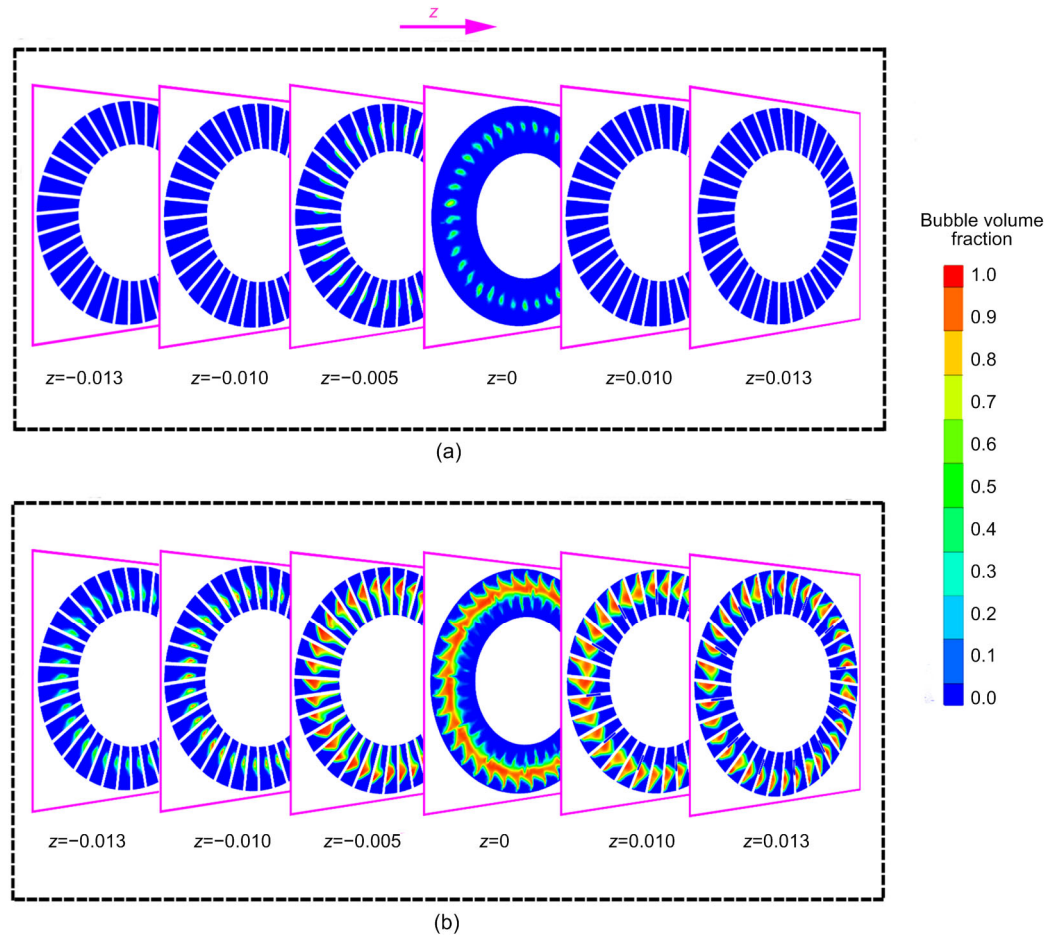


Fig. 9 Bubble distributions of the continuous axial section at 0.04 s (a) and 0.10 s (b)

sections and the bubble volume fraction is the largest on the $z=0$ surface. In addition, from the bubble distribution position, we can see that the low pressure in the center of the ring causes the volume fraction to be the largest. Otherwise, the bubble volume fractions are smaller at both ends of the ring.

The hydraulic retarder produces a vortex in the rotor and stator flow field when it operates. The left side of Fig. 10 shows the vortex in the entire flow field, and the right side is an enlarged view of the partial flow field. The arrows indicate the directions of the fluid flow, and the fluid follows the directions of the arrows and continues to circulate in the whole field. We find that there are more vortices at the intersection of the rotor and stator flow fields, where there is fluid flowing from the rotor to the stator and back to the rotor from the stator. In addition, there is a larger vortex on the suction side of the stator and rotor blades due to the lower pressure. To analyze

the variation in the flow fields with time, we extract the flow field data at 0.04 s and 0.10 s. Figs. 11a–11d analyze the radial velocity (V_r), axial velocity (V_a), turbulent kinetic energy (k), and specific dissipation rate (ω) at the extraction points. The positions of the extraction points are the same as those in Fig. 4. The velocity extraction plots in Figs. 11a and 11b show that the radial and axial velocity distributions have the same regularity. Both the radial and axial velocities at 0.10 s are larger than those at 0.04 s when r/R is relative small; however, the reverse is almost true when r/R is relative large. The turbulence data in Figs. 11c and 11d indicate that the turbulence intensity of some extraction points at 0.10 s is smaller than that at 0.04 s. These extraction points are mainly concentrated in the range of $r/R=0.25\text{--}0.70$. From the bubble volume fraction distribution in Fig. 8, we can see that this range corresponds to the center of the flow field, which is the bubble accumulation area. Therefore, we

conclude that the accumulation of bubbles will destroy the turbulent flow of the flow field, causing the turbulence intensity at 0.10 s to be smaller than that at 0.04 s and the vortex in the flow field to decrease over time.

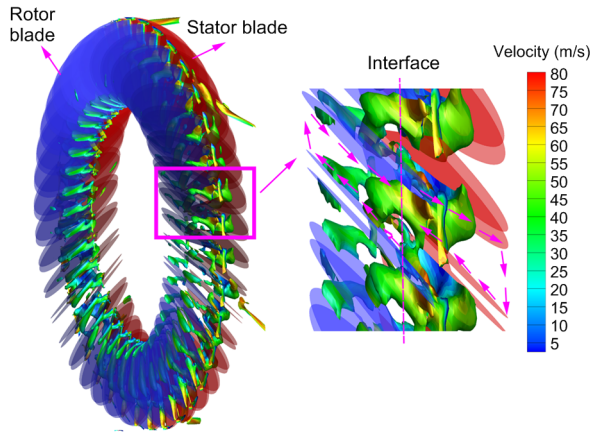


Fig. 10 Vortex distribution in the rotor and stator flow

5.3 Variation in the temperature of the rotor and stator pressure blades

The temperature changes during hydraulic operation are more obvious for the pressure blades in the rotor and the stator, so we present the temperature variation of the rotor and stator pressure blades over 0.10 s in Figs. 12a and 12b, respectively. The temperatures of the rotor and stator pressure blades gradually increase from 0.03 s to 0.10 s. Compared to the temperature changes at 0.03 s, the temperature changes at 0.10 s are more obvious. This phenomenon is caused by the fact that a large number of bubbles accumulate at 0.10 s, as shown in Fig. 8. From the rotor temperature cloud in Fig. 12a, the highest temperature is in the rotor inner diameter entrance area 1, where there is a large amount of heat due to the fluid impact. In addition, there is also an area with a high temperature distribution, as shown in area 2. The

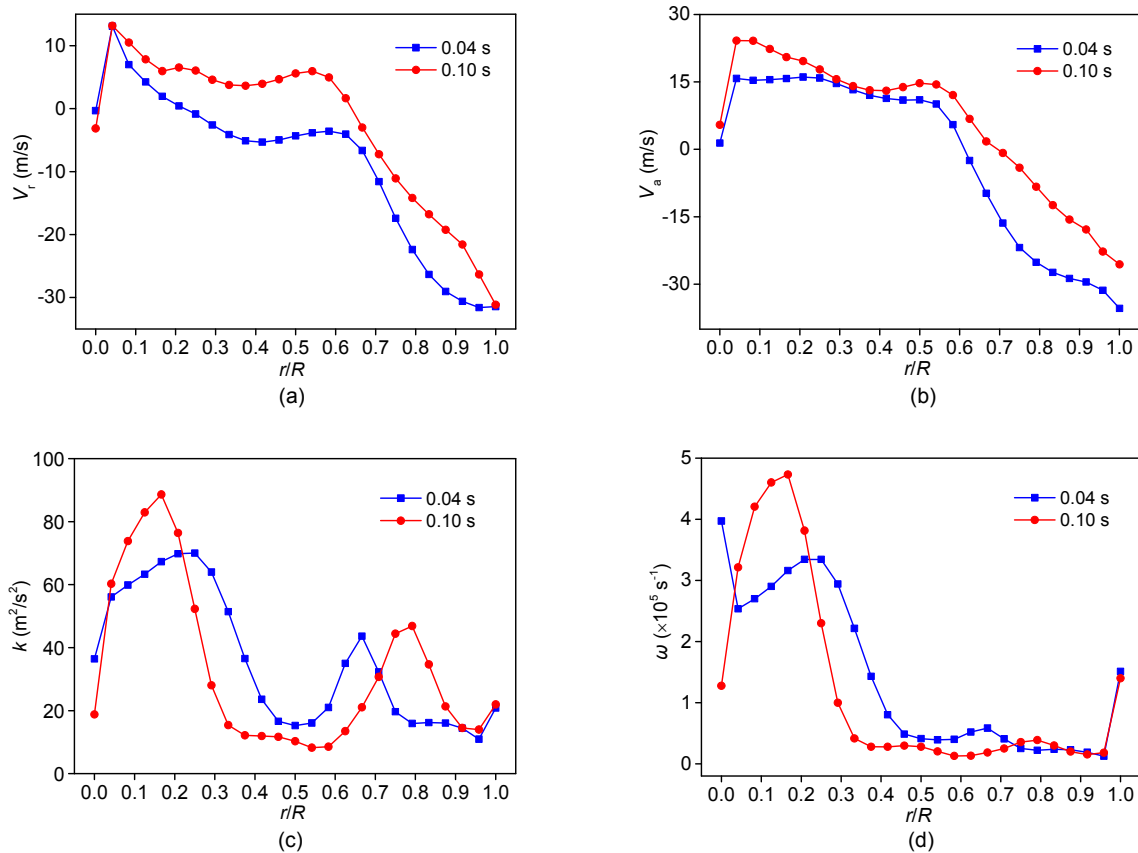


Fig. 11 Comparison of the velocity and turbulence data at 0.04 s and 0.10 s

(a) Extracted radial velocity (V_r) distribution; (b) Extracted axial velocity (V_a) distribution; (c) Extracted turbulent kinetic energy (k) distribution; (d) Extracted specific dissipation rate (ω) distribution

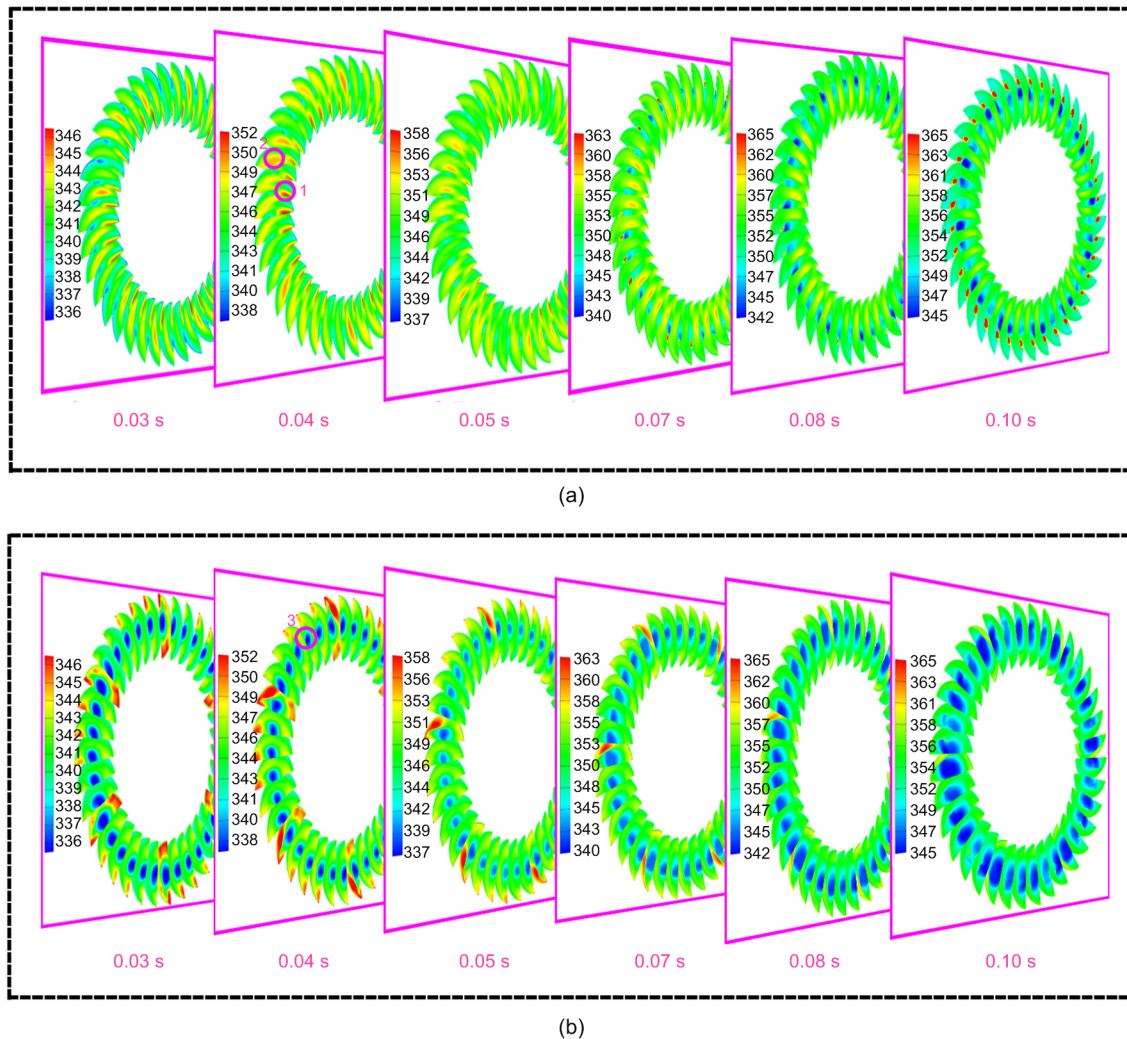


Fig. 12 Temperature cloud variations in the rotor and stator pressure blades (unit: K)
(a) Rotor blade; (b) Stator blade

lowest temperature is located in the center of the flow surface; this area is the bubble accumulation area, and thus the temperature is the lowest. Fig. 13a shows the change in the temperature of the rotor blade over time. It is found that all the highest, lowest, and average values of the temperature show an overall upward trend within 0.10 s. From the stator temperature cloud in Fig. 12b, the maximum and minimum temperature distributions in the stator are more obvious than those in the rotor. This perhaps due to the fact that more bubbles exist in the stator, as shown in Fig. 8. The lowest temperature exists in the bubble accumulation area 3 and the highest temperature is located in the outer ring area of the stator, which is subjected to a fluid impact, causing the high temperature. From the

change in the stator blade temperature over time in Fig. 13b, we find that the trend of the temperature change in the stator suction surface is more uniform. Because the heat exchange system of the retarder is not considered in the retarder modeling process and the wall of the retarder is assumed to be adiabatic, the simulated temperature of the retarder is not stable over time. From the total temperature change in Fig. 13, the maximum temperature of the rotor blade is higher than that of the stator blade due to the fluid impact; in addition, because the cavitation strength of the stator passage is stronger than that of the rotor passage when the rotational speed reaches 1200 r/min, the average temperature of the stator blade is lower than that of the rotor blade.

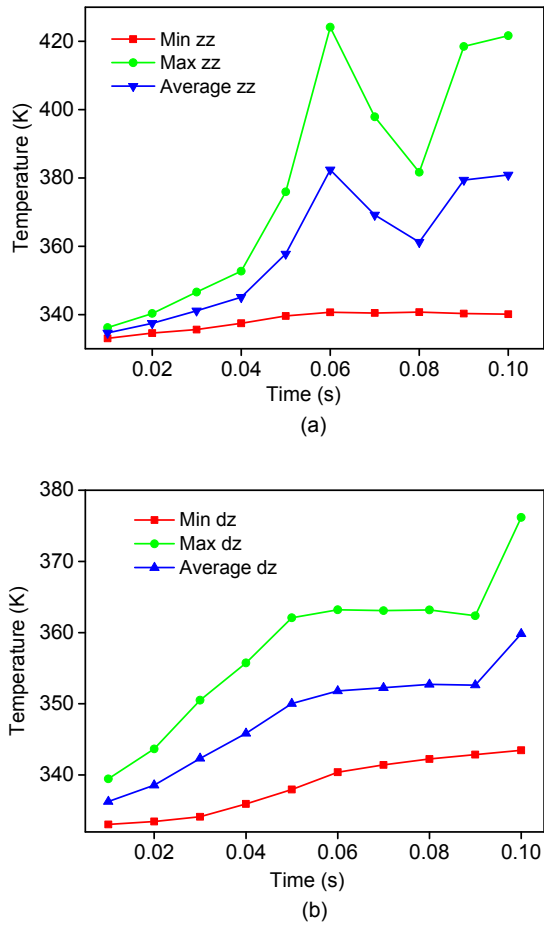


Fig. 13 Temperature changes over time of the rotor (a) and stator (b) pressure surfaces

zz represents the temperature of rotor blade; dz represents the temperature of stator blade

6 Conclusions

In this study, the IDDES, SBES, and DLES models in an SRS and the SST $k-\omega$ model in an RANS simulation were employed to simulate the flow field of a hydraulic retarder considering cavitation. The following conclusions can be summarized:

1. In the model verification, the braking torque error values of the SST $k-\omega$ model in the RANS simulation and the IDDES, SBES, and DLES models in the SRS were within 10%, and the torque error considering cavitation was smaller than that not considering cavitation. The simulation error of the SBES model was within 4%, which was also the smallest error among the four turbulence models.

2. The differences between the four turbulence models employed to simulate the flow field considering cavitation were analyzed in detail. First, the ability to capture the velocity field was fairly good for all models; however, there was an obvious difference in the simulation of the turbulence properties. The turbulence intensity simulated by the SST $k-\omega$ model was the largest, the turbulence intensity simulated by the DLES model was the smallest, and the values simulated by the SBES and IDDES models were in between these two intensities. The results of the chord vortex analysis of the flow field showed that the SBES and DLES models could effectively capture the flow field vortex; however, the SST $k-\omega$ model produced a large torque error due to excessively estimating the turbulence intensity, and the capture capability was weak.

3. Because the SBES and DLES models had a strong ability to capture details in the flow field and the simulation error of the SBES model was the lowest among the four models under high-speed conditions, we employed the SBES model to simulate the transient change in the bubble volume fraction on a typical flow surface over time. From an analysis of the bubble volume fraction distribution, the center area of the flow surface, which was a low-pressure region, was the region where the bubbles precipitated. The bubble volume fraction increased over time, and the value for the local central region reached 0.9–1.0. An analysis of the flow field data at 0.04 s and 0.10 s showed that the bubbles mainly appeared near the $z=0$ section, and it was obvious that the accumulation of the bubbles over time resulted in the turbulence intensity at 0.10 s being smaller than that at 0.04 s. During the hydraulic operation process, the blade temperature will inevitably change. An analysis of the temperature of the pressure blade showed that the temperature in the central region of the blade was lower than those in the inner and outer ring regions.

We analyzed the flow field of a hydraulic retarder considering the cavitation phenomenon and laid a theoretical foundation for future optimizations of the retarder structure to improve the performance during operation. A shortcoming of this study is that the internal cavitation flow field of the retarder could not be observed experimentally. In the next step, we would apply the particle image velocimetry (PIV) techniques to study the bubble distribution in the flow

field of the retarder and further compare the simulation abilities of different models.

Contributors

Xue-song LI designed the research. Qing-tao WU and Li-ying MIAO processed the corresponding data and wrote the first draft of the manuscript. Chun-bao LIU and Yu-ying YAN helped to organize the manuscript. Qing-tao WU and Xue-song LI revised and edited the final version.

Conflict of interest

Xue-song LI, Qing-tao WU, Li-ying MIAO, Yu-ying YAN, and Chun-bao LIU declare that they have no conflict of interest.

References

- Brennen CE, 1995. Cavitation and Bubble Dynamics. Oxford University Press, Oxford, UK, p.47-53.
- Dong Y, Korivi V, Attibele P, et al., 2002a. Torque Converter CFD Engineering Part I: Torque Ratio and K Factor Improvement through Stator Modifications. SAE Technical Paper, No. 2002-01-0883, SAE, Detroit, USA. <https://doi.org/10.4271/2002-01-0883>
- Dong Y, Korivi V, Attibele P, et al., 2002b. Torque Converter CFD Engineering Part II: Performance Improvement through Core Leakage Flow and Cavitation Control. SAE Technical Paper, No. 2002-01-0884, SAE, Detroit, USA. <https://doi.org/10.4271/2002-01-0884>
- Huang B, Wang GY, 2011. A modified density based cavitation model for time dependent turbulent cavitating flow computations. *Chinese Science Bulletin*, 56(19):1985-1992. <https://doi.org/10.1007/s11434-011-4540-x>
- Hur N, Moshfeghi M, Lee W, 2018. Flow and performance analyses of a partially-charged water retarder. *Computers & Fluids*, 164:18-26. <https://doi.org/10.1016/j.compfluid.2016.10.033>
- Liu CB, Bu WY, Xu D, et al., 2017a. Application of hybrid RANS/LES turbulence models in rotor-stator fluid machinery: a comparative study. *International Journal of Numerical Methods for Heat & Fluid Flow*, 27(12):2717-2743. <https://doi.org/10.1108/HFF-08-2016-0312>
- Liu CB, Bu WY, Wang TJ, 2017b. Numerical investigation on effects of thermophysical properties on fluid flow in hydraulic retarder. *International Journal of Heat and Mass Transfer*, 114:1146-1158. <https://doi.org/10.1016/j.ijheatmasstransfer.2017.06.124>
- Long XP, Liu Q, Ji B, et al., 2017. Numerical investigation of two typical cavitation shedding dynamics flow in liquid hydrogen with thermodynamic effects. *International Journal of Heat and Mass Transfer*, 109:879-893. <https://doi.org/10.1016/j.ijheatmasstransfer.2017.02.063>
- Luo XW, Ji B, Tsujimoto Y, 2016. A review of cavitation in hydraulic machinery. *Journal of Hydrodynamics*, 28(3):335-358. [https://doi.org/10.1016/S1001-6058\(16\)60638-8](https://doi.org/10.1016/S1001-6058(16)60638-8)
- Mejri I, Bakir F, Rey R, et al., 2006. Comparison of computational results obtained from a homogeneous cavitation model with experimental investigations of three inducers. *Journal of Fluids Engineering*, 128(6):1308-1323. <https://doi.org/10.1115/1.2353265>
- Menter FR, 1994. Two-equation eddy-viscosity turbulence models for engineering applications. *AIAA Journal*, 32(8):1598-1605. <https://doi.org/10.2514/3.12149>
- Moshfeghi M, Hur N, 2015. Effects of SJA boundary conditions on predicting the aerodynamic behavior of NACA 0015 airfoil in separated condition. *Journal of Mechanical Science and Technology*, 29(5):1829-1836. <https://doi.org/10.1007/s12206-015-0403-8>
- Orszag SA, Yakhot V, Flannery WS, et al., 1993. Renormalization group modeling and turbulence simulations. In: International Conference on Near-wall Turbulent Flows, p.139-158.
- Robinette DL, Schweitzer JM, Maddock DG, et al., 2008a. Predicting the onset of cavitation in automotive torque converters-Part I: designs with geometric similitude. *International Journal of Rotating Machinery*, 2008:803940. <https://doi.org/10.1155/2008/803940>
- Robinette DL, Schweitzer JM, Maddock DG, et al., 2008b. Predicting the onset of cavitation in automotive torque converters-Part II: a generalized model. *International Journal of Rotating Machinery*, 2008:312753. <https://doi.org/10.1155/2008/312753>
- Schnerr GH, Sauer J, 2001. Physical and numerical modeling of unsteady cavitation dynamics. Proceedings of the 4th International Conference on Multiphase Flow, p.1-8.
- Singhal AK, Athavale MM, Li HY, et al., 2002. Mathematical basis and validation of the full cavitation model. *Journal of Fluids Engineering*, 124(3):617-624. <https://doi.org/10.1115/1.1486223>
- Smagorinsky J, 1963. General circulation experiments with the primitive equations: I. The basic experiment. *Monthly Weather Review*, 91(3):99-164. [https://doi.org/10.1175/1520-0493\(1963\)091<0099:GCEWTP>2.3.CO;2](https://doi.org/10.1175/1520-0493(1963)091<0099:GCEWTP>2.3.CO;2)
- Snigirev BA, Tukmakov AL, Tonkonog VG, 2017. Numerical investigation the dynamics of vaporization at the flow of liquid methane in channel with variable section. *Journal of Physics: Conference Series*, 789:012056. <https://doi.org/10.1088/1742-6596/789/1/012056>
- Stuparu A, Susan-Resiga R, Anton LE, et al., 2010. Numerical investigation of the cavitation behaviour into a storage pump at off design operating points. *IOP Conference Series: Earth and Environmental Science*, 12:012068. <https://doi.org/10.1088/1755-1315/12/1/012068>
- Tsutsumi K, Watanabe S, Tsuda SI, et al., 2017. Cavitation simulation of automotive torque converter using a homogeneous cavitation model. *European Journal of Mechanics-B/Fluids*, 61:263-270. <https://doi.org/10.1016/j.euromechflu.2016.09.001>

- Watanabe S, Otani R, Kunimoto S, et al., 2012. Vibration characteristics due to cavitation in stator element of automotive torque converter at stall condition. ASME Fluids Engineering Division Summer Meeting Collocated with the ASME Heat Transfer Summer Conference and the ASME 10th International Conference on Nanochannels, Microchannels, and Minichannels, p.535-541. <https://doi.org/10.1115/FEDSM2012-72418>
- Zheng HP, Lei YL, Song PX, 2016. Design of the filling-rate controller for water medium retarders on the basis of coolant circulation. *Proceedings of the Institution of Mechanical Engineers, Part D: Journal of Automobile Engineering*, 230(9):1286-1296. <https://doi.org/10.1177/0954407015626637>
- Zheng HP, Lei YL, Song PX, 2017a. Hydraulic retarders for heavy vehicles: analysis of fluid mechanics and computational fluid dynamics on braking torque and temperature rise. *International Journal of Automotive Technology*, 18(3):387-396. <https://doi.org/10.1007/s12239-017-0039-z>
- Zheng HP, Lei YL, Song PX, 2017b. Water medium retarders for heavy-duty vehicles: computational fluid dynamics and experimental analysis of filling ratio control method. *Journal of Hydrodynamics*, 29(6):1067-1075. [https://doi.org/10.1016/S1001-6058\(16\)60820-X](https://doi.org/10.1016/S1001-6058(16)60820-X)
- Zheng HP, Lei YL, Song PX, 2018. Designing the main controller of auxiliary braking systems for heavy-duty vehicles in nonemergency braking conditions. *Proceedings of the Institution of Mechanical Engineers, Part C: Journal of Mechanical Engineering Science*, 232(9):1605-1615. <https://doi.org/10.1177/0954406217706386>
- Zwart PJ, Gerber AG, Belamri T, 2004. A two-phase flow model for predicting cavitation dynamics. ICMF 2004 International Conference on Multiphase Flow, Paper No. 152.

中文概要

题目：考虑气蚀的液力缓速器湍流流动尺度解析模拟

目的：液力缓速器高速运行时会产生气蚀侵蚀现象，进而对缓速器的缓速制动及平稳运行产生不利影响。本文旨在对液力缓速器的气蚀湍流场进行分析，探究气蚀侵蚀发生的原因，为进一步探究减轻气蚀侵蚀的措施提供理论基础。

创新点：1. 引入目前先进的尺度解析模拟方法来模拟湍流场，使湍流场数值计算结果更加真实；2. 采用气液两相流模型和气蚀模型相结合的方法模拟气蚀现象，并通过流场中的气泡体积来衡量气蚀侵蚀程度。

方法：1. 采用不同的湍流模型解析液力缓速器四种转速下的湍流场，并通过比较流场结果得出不同湍流模型模拟流场的区别（图 3~5 和 7）；2. 采用应力混合涡（SBES）模型模拟高转速下的气蚀流场，并提取流场处理结果来分析缓速器内部气泡体积的瞬态演变规律（图 8 和 9）；3. 提取不同时刻的叶片温度来分析气蚀引起的能量变化（图 12 和 13）。

结论：1. 在四大湍流模型中，SBES 模型模拟湍流场涡旋的能力最强且提取出的制动转矩结果与实验值最接近；2. 高转速下的气蚀侵蚀情况严重，流场中出现的气泡体积较大，并且，随着时间推移气泡体积积累对缓速器运行将产生不利影响。3. 气蚀流场中出现的气泡会影响缓速器湍流场中的涡旋，并且影响缓速器的叶片温度变化。

关键词：尺度解析模拟；液力缓速器；气蚀；非稳态流场